

## TRACING MULTIPLE GENERATIONS OF AGN FEEDBACK IN THE CORE OF ABELL 262

T. E. CLARKE<sup>1,2</sup>, E. L. BLANTON<sup>3</sup>, C. L. SARAZIN<sup>4</sup>, L. D. ANDERSON<sup>3</sup>, GOPAL-KRISHNA<sup>5</sup>, E. M. DOUGLASS<sup>3</sup>, AND NAMIR E. KASSIM<sup>1</sup>

*Draft version November 2, 2018*

### ABSTRACT

We present new radio and X-ray observations of Abell 262. The X-ray residual image provides the first evidence of an X-ray tunnel in this system while the radio data reveal that the central radio source is more than three times larger than previously known. We find that the well-known cluster-center S-shaped radio source B2 0149+35 is surrounded by extended emission to the east and south-west. The south-western extension is co-spatial with the X-ray tunnel seen in our new *Chandra* images while the eastern extension shows three clumps of emission with the innermost coincident with a faint X-ray cavity. The outer two eastern radio extensions are coincident with a newly detected X-ray depression. We use the projected separation of the emission regions to estimate a lower limit of  $\tau_{rep} = 28$  Myr to the outburst repetition timescale of the central AGN. The total energy input into the cluster over multiple outburst episodes is estimated to be  $2.2 \times 10^{58}$  ergs, more than an order of magnitude larger than previously thought. The total AGN energy output determined from our new observations shows that the source should be capable of offsetting radiative cooling over several outburst episodes.

*Subject headings:* cooling flows — galaxies: clusters: general — galaxies: clusters: individual (Abell 262) — intergalactic medium — radio continuum: galaxies — X-rays: galaxies: clusters

### 1. INTRODUCTION

The thermal gas in the cores of dense, relaxed galaxy clusters has a cooling time that is often shorter than the age of the system (Fabian & Nulsen 1977; Cowie & Binney 1977). In the absence of heating, this gas should cool through X-ray emission and be deposited within the cooling radius in the form of dense molecular clouds. Over the lifetime of the cluster, the accumulated mass could reach as much as  $10^{11} - 10^{12} M_{\odot}$ . Detailed observations over a wide range of the electromagnetic spectrum fail to detect such large quantities of cool gas deposited in cluster cores. Optical observations reveal star formation which reaches only a few percent of the predicted cooling rates in most systems (McNamara & O’Connell 1989; Cardiel et al. 1998; Crawford et al. 1999). High resolution X-ray spectroscopic observations with *XMM-Newton* show a lack of evidence for gas cooling below roughly one third of the maximum temperature (Peterson et al. 2001; Tamura et al. 2001; Kaastra et al. 2001; Sakelliou et al. 2002; Peterson et al. 2003). The lack of evidence of significant quantities of cool X-ray gas implies that the mass accretion rates to low temperatures are  $\sim 10$  times lower than previously estimated (McNamara & Nulsen 2007). One possible origin for this discrepancy is that there is a heat source in the intracluster medium (ICM) that stops significant amounts of gas from cooling to low X-ray temperatures (see review of heating mechanisms by

Conroy & Ostriker 2008).

A promising candidate for the source of heat energy in galaxy clusters is the supermassive black hole residing in the core of the central dominant galaxy. Burns (1990) found that 71 percent of cD galaxies in cooling cores showed evidence of radio outbursts associated with the central active galactic nucleus (AGN), while only 23 percent of non-cooling core cD galaxies revealed radio emission. The high spatial resolution of the Chandra X-ray Observatory has revealed the ubiquitous presence of cavities associated with radio outbursts in the cores of dense cooling core clusters (see compilations by Bîrzan et al. 2004; Dunn & Fabian 2004; Rafferty et al. 2006). The radio lobes inflated by the central AGN appear to displace the X-ray gas in the cluster core creating the depressions in the X-ray emission. These depressions provide a good means of estimating a lower limit on the mechanical energy input into the ICM by the AGN outburst. In many cases, the cavities are associated with radio emission from the current AGN outburst which can be traced at frequencies of 1400 MHz and higher. In some cases, however, there are ghost cavities that have been detected in the X-ray emission but have no radio counterpart at frequencies of 1400 MHz or higher. These cavities are generally found at projected radii much larger than the scale of the currently active radio lobes and they are thought to be the result of past outburst activity. In several individual sources, such as Perseus (Fabian et al. 2002), Abell 2597 (Clarke et al. 2005), and Abell 4059 (Clarke et al. 2007), radio observations reveal that the X-ray ghost cavities (or tunnel in the case of Abell 2597) are filled with low frequency radio emission, while in the case of Hydra A (Lane et al. 2004; Nulsen et al. 2005) an X-ray follow-up of the large low frequency outer radio lobes revealed the presence of a giant X-ray cavity.

In several cooling core systems, X-ray observations reveal the presence of multiple sets of cavities. The most

<sup>1</sup> Naval Research Laboratory, 4555 Overlook Ave. SW, Code 7213, Washington, DC 20375, USA

<sup>2</sup> Interferometrics Inc., 13454 Sunrise Valley Drive, Suite 240, Herndon, VA 20171, USA

<sup>3</sup> Institute for Astrophysical Research, Boston University, 725 Commonwealth Ave., Boston, MA 02215, USA

<sup>4</sup> Department of Astronomy, University of Virginia, P. O. Box 400325, Charlottesville, VA 22904-4325, USA

<sup>5</sup> NCRA-TIFR, Pune University Campus, Pune 411 007, India

spectacular example of a multiple cavity system is seen in the Perseus cluster (Boehringer et al. 1993; Fabian et al. 2000, 2006). Deep *Chandra* observations of this system reveal the presence of at least five individual cavities which are thought to be the remnants of past outburst episodes. Soft X-ray observations of the Virgo cluster reveal a series of filaments which trace regions that are thought to be buoyant bubbles from a series of small outbursts from the central AGN (Forman et al. 2007). In the case of the cavity system in Hydra A, Wise et al. (2007) conclude that the six observed cavities may be the result of either continuous outflow or a series of outbursts from the central AGN. In all cases, the presence of these multiple cavity systems provides new insight into the lifecycle of the central AGN.

In this paper we present detailed radio observations of the central radio source in Abell 262. The cD galaxy in Abell 262 (NGC 708) is host to a double lobed radio source B2 0149+35. Previous radio observations of this source revealed that it is a fairly weak FR I radio galaxy (Parma et al. 1986) with an ‘S’ shaped morphology and a total linear extent of  $\sim 19$  kpc. *Chandra* X-ray observations of Abell 262 by Blanton et al. (2004) showed a cavity on the eastern side of the core which was filled by 1400 MHz radio emission. Our analysis of an elliptical model-subtracted *Chandra* residual image discovered the presence of an X-ray tunnel running from the radio core to radii well beyond the western edge of the Parma et al. source (§ 3). We present detailed multi-frequency radio observations of this source which we interpret as evidence of multiple outburst episodes. Using the results of these new observations, we discuss the impact of the AGN outbursts on the surrounding ICM.

Throughout the paper we adopt the cosmological parameters  $H_o = 71$  km s $^{-1}$  Mpc $^{-1}$ ,  $\Omega_\Lambda = 0.73$ , and  $\Omega_m = 0.27$ . At the redshift of Abell 262 ( $z = 0.0163$ ) this cosmology corresponds to a scale of 0.327 kpc/”.

## 2. OBSERVATIONS

Low frequency radio observations of Abell 262 were undertaken with the National Radio Astronomy Observatory’s (NRAO) Very Large Array (VLA) operating at two frequencies near 325 MHz and the Giant Metrewave Radio Telescope (GMRT) operating at frequencies near 235 and 610 MHz. VLA data obtained at frequencies near 1400 and 4500 MHz are also included in the analysis presented here. Table 1 provides the details of the radio observations discussed in this paper.

### 2.1. VLA Data

VLA radio observations of B2 0149+35 were taken at frequencies around 1400 and 330 MHz with the VLA in A configuration. At 330 MHz these observations (obtained 2003 July 27) provide a resolution of  $\sim 6''$ , while at 1400 MHz (obtained 2000 December 19) the resolution is  $\sim 1.5''$ . The source 3C48 was observed as a calibrator for the 330 MHz observations and was used for bandpass, flux, and phase calibration of the target. The 330 MHz data were obtained in spectral line mode to permit excision of radio frequency interference (RFI) and avoid problems of bandwidth smearing. The 1400 MHz A configuration data were taken in continuum mode and used 3C147 as a flux calibrator and 0201+365 as a phase calibrator. These observations were supplemented by VLA

archival observations at 1400 MHz from B and C configurations (taken in 2005 April 16 and 1997 September 18, respectively) to provide sensitivity to extended low surface brightness emission. The B configuration 1400 MHz data was taken in spectral line mode and used 3C48 as bandpass, flux, and phase calibrator. The C configuration observations were obtained in continuum mode and used 3C48 as a flux calibrator and 0119+321 as a phase calibrator. Observations at 4500 MHz in the VLA D configuration on 2000 October 1 were also reduced in order to obtain total flux information for the integrated spectrum of the source. These observations were taken in continuum mode and had 3C286 as a flux calibrator and used 0145+386 as a phase calibrator.

The data were calibrated and reduced with the NRAO Astronomical Image Processing System (AIPS). Images were produced through the standard Fourier transform deconvolution method. All data sets were processed through several loops of imaging and self-calibration to reduce the effects of phase and amplitude errors in the data. Frequencies near 1400 MHz and below were reduced using the wide-field imaging capabilities within the AIPS task IMAGR. The two frequencies near 330 MHz were combined together to make the final image. Similarly all frequencies and configurations for the 1400 MHz data were combined into the final image.

### 2.2. GMRT Data

Abell 262 was observed with the GMRT on 2004 July 24. The observations were taken in dual frequency mode providing two single polarization (Stokes RR) frequencies near 610 MHz and one single polarization (Stokes LL) frequency near 235 MHz. The 610 MHz observations had a bandwidth of 16 MHz for each frequency resulting in a total bandwidth of 32 MHz and a resolution of  $\sim 6''$ . The total bandwidth of the 235 MHz data was 8 MHz and the resolution is  $\sim 13''$ . All data were taken in spectral line mode to allow RFI excision and reduce problems of bandwidth smearing. At both frequencies we used 3C48 as bandpass, flux, and phase calibrator.

The GMRT data reductions were carried out with AIPS. The GMRT data near 610 MHz were fairly clear of interference while the 235 MHz data required a significant effort to flag the RFI. The calibration followed standard wide-field imaging techniques and both data sets were self-calibrated through several loops of phase and amplitude calibration. The two frequencies near 610 MHz were calibrated and imaged separately and the final combined image was made using the image plane deconvolution task APCLN within AIPS.

### 2.3. Chandra Data

Abell 262 was observed by *Chandra* on 2006 November 20 (ObsID 7921) and 2001 August 3 (ObsID 2215) for 111,934 s and 30,305 s respectively. For each observation, the center of the cluster was positioned on the back-illuminated ACIS-S3 detector with the events telemetered in very faint (VF) mode and an energy filter of 0.1 – 13 keV. The cluster centroid was positioned with a 1’ offset from the nominal pointing to avoid node boundaries. The “level 1” events files were processed with CIAO version 3.4 following the standard procedure for VF mode. Only events with ASCA grades 0, 2, 3,

4, and 6 were included. By analyzing light curves of the two back-illuminated detectors (ACIS-S1 and ACIS-S3) throughout the observation period, it was determined that no background flares occurred to contaminate the data. The data were corrected for hot pixels and cosmic-ray afterglows using standard techniques. The resulting cleaned exposure times were 110,674 s and 28,744 s.

A merged image of both pointings (chips ACIS-S2, ACIS-S3, and ACIS-S4) was created by reprojecting the event files of the older ObsID 2215 to the WCS reference frame of our new deeper observations (ObsID 7921). This resulted in a total combined exposure time of 139,418 s. Energy was restricted within the range of 0.3-10.0 keV. Background files were taken from the blank sky observations of M. Markevitch included in the CIAO calibration database (CALDB) and reprojected to match both observations of A262. The background files for both pointings were then merged using ObsID 7921 as a reference. Matching exposure maps were created for each observation and merged in a similar manner.

### 3. X-RAY ANALYSIS

A detailed discussion of the the cluster properties based on the new merged *Chandra* data, including spectral fitting, will be presented in Blanton et al. (2009). For a review of the cluster properties based on the original short *Chandra* observations see Blanton et al. (2004). Here, we concentrate on details of the central region of the cluster. Using IRAF, we fit a smooth elliptical model to the Gaussian smoothed ( $\sigma = 5''$ ) background and exposure corrected 0.3 – 10 keV merged image of Abell 262. The ellipticity, position angle, and intensity of the isophotes were allowed to vary about the fixed X-ray centroid. In Figure 1 we show the residual image of the cluster center resulting from subtracting the elliptical model from the Gaussian smoothed image. In addition to the inner eastern X-ray hole discussed in Blanton et al. (2004), the residual image also reveals the first evidence of an X-ray tunnel to the west of the cluster core.

The inner eastern cavity is significant at the  $22 \sigma$  level and appears to be nearly completely surrounded by a bright X-ray rim while the newly discovered western tunnel appears to have only a partial rim. We have extracted counts in an annulus with inner and outer radii equal to the distance from the AGN of the inner and outer edge of the tunnel region, respectively, and excluded the counts from the tunnel region itself for the annulus counts. Comparison of the counts in this region to the counts in the tunnel feature reveals that the tunnel is significant at the  $11 \sigma$  level. Aside from these two most prominent features, the residual image also shows evidence of the faint eastern cavity discussed in Blanton et al. (2004) (marked with dashed circle). Analysis of the new merged *Chandra* data shows that this feature is still of low significance compared to X-ray counts at a similar radius. The residual image also shows a deficit to the north of the cluster core that is significant at roughly the  $8 \sigma$  level. This deficit is located between two bright X-ray knots that are associated with [N II] emission (Plana et al. 1998) and may either be a signature of a clumpy ICM or an additional X-ray cavity. Further to the east of the cluster core there appears to be a previously unknown extended X-ray deficit surrounded by a faint X-ray rim. Analysis of this extended complex

region shows that it is significant at only the  $2 \sigma$  level.

## 4. MULTI-FREQUENCY RADIO ANALYSIS

### 4.1. Morphology

In Figure 2 we show the VLA B configuration 1400 MHz image of B2 0149+35. The central radio emission contains a compact core connected to a western extension which may trace the western radio jet. A bright region to the east of the core may be associated with the counterjet which would suggest an initial position angle of  $\sim 65^\circ$  (from north to the east) for the jet axis. Beyond the bright central regions the radio emission extends into the western and eastern radio lobes. The outer lobes lie at a different position angle through the core as compared to the bright jet and counterjet. This variation in the source position angle may indicate bulk rotation of the surrounding ICM such as suggested by Gopal-Krishna & Saripalli (1984) for Centaurus A. Numerical simulations of the impact of bulk ICM motions on embedded radio galaxies reveal that such motions can reproduce observed radio galaxy morphologies (Heinz et al. 2006). An alternative explanation for the structure of B2 0149+35 is that the position angle of the radio jets has precessed over time as suggested for clusters such as Perseus (Dunn et al. 2006), RBS797 (Gitti et al. 2006) and Abell 2626 (Wong et al. 2008).

Blanton et al. (2004) showed that the eastern radio lobe is coincident with the inner eastern cavity seen in the *Chandra* data. Figure 2 shows that in addition to the S-shaped radio source, there is a compact radio source located  $\sim 17$  kpc east of the core of B2 0149+35. This source has no X-ray counterpart and no known optical identification but seems to be located near the eastern edge of a faint optical source on the Second Generation Digitized Sky Survey (DSSII) images. The total radio flux of the compact source at 1400 MHz is  $0.67 \pm 0.17$  mJy. Although the low signal to noise on this source makes the calculation of the spectral index uncertain, we note that it is consistent with that of typical extragalactic sources.

Combining the A, B, and C configuration 1400 MHz data allows us to trace more extended radio emission from B2 1049+35 since these data are sensitive to lower surface brightness emission. Figure 3A shows the combined three configuration data set as contours overlaid on the central region of the residual *Chandra* image. We note the presence of bright X-ray clumps to the north-east and south-west of the radio core at roughly the projected location where the radio jets change position angle. Higher resolution radio data of the jets would help determine if there is a connection between the X-ray clumps and the jet deflection. The entire radio source appears to be fully confined by the bright X-ray rims seen in the residual *Chandra* image.

The radio emission shown in Figure 3A extends further to the west and north-west of the radio core than is seen by Parma et al. (1986). Beyond the north-west emission there is a further radio extension to the southwest, along the X-ray tunnel. The radio emission appears to be continuous from the core toward the north-west to a distance of  $\sim 34''$  ( $\sim 11$  kpc) at which point it appears to break up into two connected clumps to the south-west within the tunnel. Both clumps reveal extended structure and do

not have any optical identifications; thus they are most likely tracing radio plasma ejected from the central AGN in NGC 708. At the lowest contour level ( $3\sigma$ ) the western emission does not reveal an obvious sharp edge to the source suggesting that we may not be tracing the full extent of the emission at this frequency. The emission to the east, beyond the counterjet location, fills the inner eastern X-ray cavity and appears to have a relatively well defined edge.

Lower frequency full-resolution radio observations at 610 MHz from the GMRT highlight again the close confinement of the synchrotron emission by the bright X-ray rims seen in the *Chandra* image (Figure 3B). These new radio data also confirm the presence of extended radio emission tracing the southwest X-ray tunnel and show that the emission extends further down the tunnel at this frequency. They also reveal diffuse emission running from the eastern radio lobe to the region south of the compact radio source. This eastern emission is coincident with the location of the faint ghost cavity mentioned in Blanton et al. (2004) and thus supports the interpretation of this region as an X-ray cavity. The total flux in the eastern extension (excluding the compact source) is  $5.3 \pm 0.5$  mJy.

We have also analyzed the 610 MHz data applying a suitable taper to the  $uv$  distribution to produce a map sensitive to the large scale diffuse emission. The taper was chosen to allow us to match the  $13''.1$  beam of our lowest frequency observation at 235 MHz. The tapered 610 MHz image (Figure 4A) reveals radio emission extending the full length of the tunnel and shows a series of connected clumps of emission running  $\sim 22$  kpc eastward (in projection) from the eastern X-ray cavity. These previously unknown radio clumps are coincident with the newly detected extended outer eastern cavity discussed in Section 3. An inspection of the DSS images shows that there are no apparent optical counterparts to the eastern emission regions. The total (projected) linear extent of the radio emission at 610 MHz is  $\sim 60$  kpc, more than 3 times larger than previously reported by Parma et al. (1986). Similar evidence of larger source sizes at low frequencies has been seen in other cluster-center radio sources such as M87 (Owen et al. 2000), Perseus (Fabian et al. 2002) and Hydra A (Lane et al. 2004) where the large outer structures have been interpreted as signatures of one or more past AGN outbursts. The clumpy morphology of the eastern emission and total extent of the radio emission in Abell 262 is also seen in Figure 4B where we show the VLA 330 MHz data convolved to the same resolution as the tapered 610 MHz data.

Our lowest frequency observations at 235 MHz are shown in Figure 4C. These data also trace the western radio emission over the full length of the X-ray tunnel. On the eastern side of the source, the 235 MHz observations reveal radio emission located well beyond the eastern compact source out to the edge of the 610 MHz extensions seen in Figure 4A. At the  $3\sigma$  contour level this emission does not show a continuous connection to B2 0149+35 but this is likely due to the lower sensitivity of the 235 MHz data.

#### 4.2. Spectral Index

We have made a spectral index map of the central radio source using the 235 and 610 MHz GMRT data. The  $uv$ -coverage of both data sets was matched and both frequencies were imaged with a circular  $13''.1 \times 13''.1$  beam. We show this spectral index map in Figure 5 where we have blanked the spectral index map at the  $3\sigma$  level on each of the input maps. The colorbar at the top shows the (linear) spectral index scale running from  $\alpha = -3.0$  to  $\alpha = -0.4$ , where  $S_\nu \propto \nu^\alpha$ . We have overlaid the 610 MHz tapered contours in white on Figure 5 to provide a reference for the source morphology in the locations where we have measured the spectral index. Typical uncertainties in the flux measurements due to calibration and systematic errors at the GMRT are of the order of 5% at 235 and 610 MHz (Lal & Rao 2006), resulting in a typical error on the spectral index of  $\sigma_\alpha = 0.2$ .

The spectral index in the area of the radio core is fairly flat ( $\alpha = -0.5$ ) which is typical of recently injected particles. The spectral index toward the western part of the source steepens away from the core reaching a value of  $\alpha = -1.7$  in the region of the X-ray tunnel. The integrated spectral index of the radio emission in the tunnel is  $\alpha_{235}^{610} = -1.3 \pm 0.2$ . The origin of the apparent spectral flattening of the emission on the western edge of the tunnel is uncertain and may be a result of low signal to noise at the edge of the 235 MHz image since the apparent steepening is within roughly the  $3\sigma$  errors on the spectral index map. Toward the eastern edge of the source the spectral index steepens less dramatically away from the core reaching  $\alpha_{235}^{610} = -0.9$ . The region of the eastern radio clumps shows an even steeper spectral index of roughly  $\alpha_{235}^{610} = -1.8$ . Although we cannot use the current data to trace small spectral index variations accurately across the source, we note that the spectral steepening observed from the core toward the outer source edges is significant above the  $3\sigma$  level and likely traces spectral aging of the relativistic particles as they travel further from the core. We have also made spectral index maps using the 330 MHz and 1400 MHz images and find similar evidence of spectral steepening away from the core in those maps.

#### 4.3. Integrated Spectrum

The spectral index determined for the full source measured from our observations between 235 and 4535 MHz is  $\alpha = -0.90 \pm 0.16$ , where we have assumed an uncertainty of 5% on the GMRT 235 MHz flux, and 1% on the VLA 4535 MHz flux. Assuming a similar flux uncertainty of 5% on the GMRT 610 MHz observations we find an integrated low frequency spectral index of  $\alpha = -0.71 \pm 0.17$  between 235 and 610 MHz. These observations suggest a possible flattening of the radio spectrum to low frequencies but we note that this cannot be confirmed from these data due to the relatively large errors on the GMRT flux estimates. We have searched the literature for total flux measurements of B2 1049+35 in order to determine the overall spectral shape of the radio emission. We list the available flux measurements in Table 2 and plot the radio spectrum including both our new measurements and the data from the literature in Figure 6. Several of the measurements from the literature were obtained with sufficiently large beams that the measured flux is contaminated by sources surrounding B2 0149+35. These measurements are marked with triangles in the figure.

The shape of the radio spectrum can be used to estimate the age of the source by using models to fit the balance of energy injection and losses. Although the available flux measurements for B2 0149+35 cover roughly a factor of 65 in frequency, they still do not sample a large portion of the radio spectrum. We have fit all measurements in Table 2 to several particle injection models to determine the break frequency<sup>6</sup> of the emission of the full source. The fits were done for both the full sample of flux measurements and also the subset of uncontaminated flux measurements. The three models used to fit the data were the JP (Jaffe-Perola), KP (Kardashev-Pacholczyk) and CI (continuous injection) spectral models. The JP and KP models both assume a single “one-shot” injection of a power-law distribution of electrons with no further acceleration (Jaffe & Perola 1973; Kardashev 1962; Pacholczyk 1970). The JP model allows for pitch-angle scattering, resulting in an exponential cutoff in the emission spectrum, while the KP model does not allow pitch-angle scattering and thus has an emission spectrum consisting of two power-laws. The CI model assumes a continual injection of a power-law distribution of relativistic particles resulting in a spectral break that changes by  $-0.5$  in  $\alpha$ . All three models produce similar fits to the data and predict the break frequency lies in the range of 1400 to 9600 MHz. We find similar spectral break frequencies if we include or exclude the contaminated flux measurements from the literature. We have also separately fit the break frequency for the bright emission filling the eastern cavity as well as the fainter emission in the tunnel and to the east of the X-ray cavity. These regions were fit using only the data presented in this paper as the individual regions needed to be isolated to determine the fluxes. The break frequency in the bright regions is between 2200 and 12000 MHz while in the fainter extended emission it is between 1900 and 7400 MHz. For all models we assume an initial injection spectrum of  $\alpha = -0.6$  which is the measured spectral index of the source between 330 and 610 MHz.

The average radiative age of the synchrotron emission is given by Miley (1980) as:

$$\tau = 0.82 \frac{B^{0.5}}{B^2 + B_{IC}^2} [(1+z)\nu_b]^{-0.5} \text{ yr} \quad (1)$$

where  $B$  is the magnetic field strength in the source in Gauss,  $B_{IC}$  is the equivalent magnetic field strength of the microwave background [ $4 \times 10^{-6}(1+z)^2$  Gauss], and  $\nu_b$  is the break frequency in GHz. Assuming a break frequency at the low end of the model predictions of 1400 MHz and that the source field strength is  $B = B_{IC}/\sqrt{3}$  to give the maximum radiative lifetime (van der Laan & Perola 1969), we estimate the age of B2 0149+35 as  $\sim 47$  Myr. If the break frequency is near the high end from the spectral fits (9600 MHz), we then obtain a younger age of  $\sim 18$  Myr.

## 5. RADIO LOBE INTERACTION WITH THE ICM

The central radio source in Abell 262 appears to have had a significant impact on the thermal gas distribution in the center of this cluster. Blanton et al. (2004) showed

the cluster core contains several knots of X-ray emission as well as at least one X-ray cavity to the east of the radio core while our new residual *Chandra* image reveals the presence of an X-ray tunnel running westward from the AGN as well as an extended outer eastern cavity (Figure 1). We use our observations of the synchrotron emission to obtain estimates of the radio properties for comparison with the surrounding thermal gas properties.

### 5.1. ICM Pressure Balance

The western extension along the X-ray tunnel is fairly faint at 1400 MHz and thus the spectral index of the extension is not well constrained at high frequencies. In § 4.2 we estimate the low frequency spectral index of the emission in the tunnel to be  $\alpha_{235}^{610} = -1.3 \pm 0.2$ . We use this spectral index measurement together with the flux measurement at 610 MHz to estimate the minimum energy properties of the western radio extension. We follow the notation of Miley (1980) and assume that the emission from the western extension comes from a uniform prolate cylinder with a filling factor ( $f$ ) of unity and that there is equal energy in relativistic ions and electrons ( $\kappa = 1$ ). We use a source size of  $\sim 16.5 \times 6.0$  kpc and a model where the magnetic field is perpendicular to the line of sight and the spectral index is constant between the lower cutoff frequency of 10 MHz and the upper frequency cutoff of 100 GHz. Using these parameters for the tunnel, we calculate a minimum energy magnetic field strength of  $B_{me} = 5.0 \mu\text{G}$ , a non-thermal pressure of  $P_{me} = 1.4 \times 10^{-12} \text{ dyn cm}^{-2}$  and a synchrotron lifetime at 1400 MHz of  $\tau_{me} = 37$  Myr. Note that adiabatic expansion reduces the loss rate of the relativistic electrons, and as a result the synchrotron lifetime may be shorter than derived from the observed radio properties.

The X-ray gas pressure in the region surrounding the tunnel is estimated from the *Chandra* observations to be  $P_X = 6.4 \times 10^{-11} \text{ dyn cm}^{-2}$ . This X-ray pressure is more than 25 times larger than our estimated minimum energy synchrotron pressure. This discrepancy between the synchrotron and X-ray pressure is typical of many cooling core systems as shown by Dunn et al. (2005). Similar pressure discrepancies are found in the case of lobes associated with several more powerful FR II sources as well (e.g. Hardcastle & Worrall 2000). Such a pressure difference cannot be physical since it would result in a rapid collapse of the radio lobes. This may suggest that the assumptions used in our minimum energy calculations are wrong. Equipartition between the synchrotron plasma and thermal gas would require  $\kappa/f=260$ , which would suggest that the lobes are fed by heavy jets. An alternative solution to the pressure discrepancy is that there is an additional form of pressure support in the lobes (e.g. a very hot diffuse thermal gas).

The synchrotron emission coincident with the outer eastern X-ray cavity has a spectral index ranging from  $\alpha = -1.0$  to as steep as  $\alpha = -1.5$  between 235 and 610 MHz. Using the flatter spectral index and the minimum energy assumptions above, we estimate a minimum energy magnetic field strength of  $B_{me} = 2.6 \mu\text{G}$ , a non-thermal pressure of  $P_{me} = 4.1 \times 10^{-13} \text{ dyn cm}^{-2}$  and a synchrotron lifetime (neglecting adiabatic expansion) at 1400 MHz of  $\tau_{me} = 46$  Myr. We estimate an average X-ray pressure of  $P_X = 5 \times 10^{-11} \text{ dyn cm}^{-2}$  in the same region as the synchrotron emission. As discussed above,

<sup>6</sup> The break frequency is the frequency above which the synchrotron emission spectrum steepens due to particle losses.

this pressure difference cannot be physical and likely indicates either incorrect minimum energy assumptions or the presence of an additional form of pressure support within these regions.

### 5.2. Buoyant Rise Time in the X-ray Tunnel

If the western radio extension represents a buoyant lobe from a previous outburst then we can estimate the buoyancy rise time for the lobe to reach the end of the tunnel. The sound speed in the thermal gas is  $c_s = \sqrt{\frac{\gamma kT}{\mu m_H}}$  where  $\gamma = 5/3$  is the adiabatic index of the gas,  $T$  is the X-ray temperature of the gas,  $\mu$  is the mean molecular weight of the gas, and  $m_H$  is the mass of the proton. Using  $T = 1\text{keV}$  from Blanton et al. (2004), the sound speed in the central cluster region is  $c_s = 475\text{ km s}^{-1}$ . As the lobe rises it will approach a terminal velocity that is determined by the balance of buoyancy and drag forces. Based on the terminal velocity approach of Churazov et al. (2001), McNamara & Nulsen (2007) give the terminal velocity in terms of the Kepler speed ( $v_K$ ) as  $v_b \propto (4v_k/3)(2r/R)^{0.5}$ , where  $r$  is the bubble radius,  $R$  is the bubble distance from the cluster center and the Kepler speed is given by  $v_K = (gR)^{0.5}$ . The local gravitational acceleration,  $g$ , can be estimated from the local stellar velocity dispersion assuming the galaxy is an isothermal sphere,  $g \simeq 2\sigma^2/R$ . The stellar velocity dispersion for NGC 708 is given by Bernardi et al. (2002) as  $235\text{ km s}^{-1}$ , which results in a terminal velocity of  $v_b = 245\text{ km s}^{-1}$  for the outer bubble.

Based on the above terminal velocity, we find a buoyant lobe would reach the observed (projected) location at the end of the tunnel on a timescale  $\tau_{buoy} \gtrsim 80\text{ Myr}$ . Note that the lower limit on the buoyancy timescale is due to projection since the radio structure may not be in the plane of the sky. On the other hand, if the tunnel remains evacuated of thermal ICM between successive outbursts then the rise time calculated above overestimates the timescale for the synchrotron emitting plasma to reach the end of the tunnel. We cannot make a firm statement regarding the need for particle re-acceleration in the tunnel due to the uncertainties in the estimates of the synchrotron lifetime of the particles in the tunnel (§ 5.1) as well as the uncertainties in the buoyancy rise time.

### 5.3. AGN Outburst Timescale

The radio emission on the eastern side of the core (beyond the eastern lobe) likely represents emission from one or more previous outburst episodes from the central AGN. We measure projected distances from the center of the eastern cavity of  $\sim 10, 17,$  and  $21\text{ kpc}$  for the three eastern structures. Assuming that each of these represents a buoyant lobe from a past AGN outburst and using the calculated terminal velocity of the buoyant bubbles ( $v_b = 245\text{ km s}^{-1}$ ), we can estimate the outburst repetition rate in this system to be  $\tau_{rep} \sim 28\text{ Myr}^7$ . This outburst timescale is similar to the esti-

<sup>7</sup> Note that we chose to use the distance from the center of the eastern cavity for three outbursts rather than the cluster core and four outbursts since it is unlikely that the inner active lobe has been rising at the terminal velocity while this is likely a good approximation for the outer detached lobes.

mate for Perseus using the observed spacing of the X-ray ripples (Fabian et al. 2003). Such a short repetition timescale would suggest that multiple outbursts may be responsible for creating the emission seen in the tunnel. We note that it seems unlikely that the repetition rate is as long as the typically assumed  $10^8\text{ yr}$  since buoyancy arguments would require the bubbles to be aligned at an inclination of less than  $20^\circ$  from the line of sight. An alternative interpretation for the new radio morphology is that the three eastern clumps may represent a much larger fragmented bubble from a single outburst that occurred prior to the current activity powering the inner lobes. In this case (even without considering projection effects) our repetition timescale would be an underestimate of the true repetition timescale.

### 5.4. Energy Balance: Total AGN Input vs Cooling Luminosity

Our new radio observations of B2 0149+35 show significant structure in the radio source to the east of the X-ray cavity. Interpreting the synchrotron emission as a series of buoyantly rising bubbles from past radio outbursts allows us to obtain a lower limit on the total energy input into the ICM over at least four outburst episodes in this source. We assume that the bubbles rise buoyantly and undergo adiabatic expansion in pressure equilibrium with the surrounding thermal gas. Following the notation of Churazov et al. (2002), the initial energy input from the outburst is related to the final bubble properties by

$$E_o = \frac{\gamma}{\gamma - 1} p_f V_f \left( \frac{p_o}{p_f} \right)^{\frac{\gamma - 1}{\gamma}} \quad (2)$$

where  $\gamma$  is the adiabatic index of the plasma in the lobes,  $p_o$  is the initial ambient pressure where the lobe was originally inflated,  $p_f$  is the surrounding pressure at the current location of the buoyant lobe, and  $V_f$  is the volume of the bubble at the current location. Due to sensitivity limitations, X-ray depressions are difficult to isolate for all radio features of B2 0149+35 and thus the cavity volumes are estimated based on the observed synchrotron emission seen at  $610\text{ MHz}$ . The radio emission is less sensitive to projection effects than X-ray depressions (as also noted by Birzan et al. 2008).

The A262 cavity system provides us with the opportunity to estimate variations in outburst energies over several episodes for the same AGN. We have separated the radio source into 7 components (4 east of the core and 3 west of the core; Figure 7) and calculated the initial input energy from the AGN required to create these regions. The inner (spherical) eastern cavity was defined based on the X-ray cavity size and morphology. We use the same bubble shape and volume to match the inner western cavity while the remainder of the western X-ray tunnel is represented by a prolate cylinder. At the end of the western tunnel we define a small prolate cylinder based on the radio morphology. The outer eastern components were defined based on the radio morphology visible above the  $5\sigma$  level. The first component is spherical while the outer two components are represented by prolate cylinders. The bubbles were assumed to be initially inflated at a radius consistent with that of the active eastern radio lobe and associated X-ray cavity. Using the location of the active eastern cavity rather than the cluster center

as the inflation and detachment point avoids complications from likely supersonic or transonic jets closer to the cluster core. The X-ray pressure surrounding each region was determined from the radial profile obtained from the *Chandra* observations.

In Table 3 we present a summary of the sizes and initial input energies calculated for each component. The lower limit on the initial energy input varies from  $\sim 5 \times 10^{56}$  ergs up to  $\sim 8 \times 10^{57}$  ergs, while the total energy summed over all 7 radio components is  $2.2 \times 10^{58}$  ergs. This total energy input is similar to the average energy calculated for typical ‘single’ outburst systems (Birzan et al. 2004). From the results in Table 3 we find that the current epoch of activity from B2 0149+35 is the most energetic if our underlying assumptions on the origin of the radio morphology hold. In fact, the distribution of the outburst energy for each of the components of the source shows that the energy appears to be roughly consistent with a continual increase to the current epoch. Such an increase in outburst energy may be the signature of a system where the cooling luminosity continues to dominate over the AGN energy injected into the ICM leading to an increase in the fueling of the AGN with time and thus more energetic outbursts. The observed trend in outburst energy for B2 0149+35 is different from that seen for the multicavity system in Hydra A (Wise et al. 2007). In that case, Wise et al. (2007) find that the energy required to create the outer cavities is nearly an order of magnitude larger than that for the inner cavities. We also note that the cavity size trend for B2 0149+35 seen in Table 3 does not follow the bubble size versus radius trend seen in the cavity sample of Diehl et al. (2008).

Based on the radio morphology, we suggest that the source components are the result of 4 outburst episodes that have a repetition time of  $\sim 28$  Myr. The total AGN kinetic luminosity over these outbursts is  $L_{AGN} = 6.2 \times 10^{42}$  ergs  $s^{-1}$ . Blanton et al. (2004) estimate the cooling luminosity in A262 to be  $L_{cool} = 1.3 \times 10^{43}$  ergs  $s^{-1}$ , which is roughly a factor of two higher than the estimated AGN kinetic luminosity. Although Blanton et al. showed that the current radio outburst is apparently too weak to offset cooling assuming  $\tau_{rep} = 10^8$  yr, our new data suggest that the AGN in NGC 708 can offset cooling on average with our shorter repetition timescale over the observed multiple outburst episodes. If the eastern radio morphology is instead the result of fragmentation from a single outburst episode it is likely that the energy output estimate above would underestimate the true AGN output.

### 5.5. Radiative Efficiency

The presence of the intracluster medium confining the radio lobes allows us to compare estimates of the kinetic energy of the radio jets to the observed bolometric radio luminosity of the system. The radiative efficiency determined from embedded AGNs provides important insights into the impact of AGN outbursts on the evolution of the host galaxy and the intracluster medium as well as information relating to AGN accretion and jet formation models. Theoretical estimates of the radiative efficiency fall in the range of 5 – 10% (De Young 1993; Bicknell 1995). An observational estimate of the radiative efficiency of 10% was obtained by Wold et al. (2007) using a sample of FRI and FRII sources from the 3CRR catalog

of Laing et al. (1983). Using a sample of radio sources associated with cluster-center cavities, Birzan et al. (2004) find the radiative efficiencies fall in the range of a few tenths of a percent to a few percent.

The total radio luminosity of B2 0149+35 was calculated by integrating the flux between 10 MHz and 10 GHz assuming a constant spectral index of  $\alpha = -0.90$  and the total flux as measured from our 235 MHz observations. We find the bolometric radiative power to be  $L_{radio} = 3.9 \times 10^{39}$  ergs  $s^{-1}$ , roughly 50% higher than the bolometric luminosity calculated in Birzan et al. (2008). A lower limit on the total AGN energy output is obtained from the mechanical power deposited into the ICM from this radio source ( $pV$  work) divided by the timescale for the energy input. From § 5.4 we estimate the total AGN kinetic luminosity to be  $L_{AGN} = 6.2 \times 10^{42}$  ergs  $s^{-1}$ , giving a radiative efficiency similar to Birzan et al. (2004) of  $\sim 0.1\%$ , reinforcing the view that this source appears to be a very inefficient radiator.

### 5.6. Mass Accretion Rate

The inferred black hole mass for B2 0149+35 can be calculated using the velocity dispersion versus black hole mass relation of Tremaine et al. (2002). The stellar velocity dispersion of 235 km  $s^{-1}$  for NGC 708 (Bernardi et al. 2002) corresponds to a black hole mass of  $2.6 \times 10^8 M_{\odot}$ . The total energy output estimated for the four outburst episodes traced by the radio emission implies an average accretion rate of 0.001  $M_{\odot}$   $yr^{-1}$  assuming  $\epsilon = 0.1$  as the efficiency of converting accreted mass to kinetic energy outflow. This mass accretion estimate is similar to that determined by Rafferty et al. (2006) from the analysis of only the inner X-ray cavities in Abell 262.

## 6. SUMMARY

We have undertaken a detailed multi-frequency radio study of B2 0149+35 which is associated with the cluster-center galaxy in Abell 262. Our new low frequency radio observations reveal that the source is nearly three times larger than previously known. The S-shaped source seen by Parma et al. (1986) is surrounded by emission to the east and west. The western emission extends from the edge of the Parma et al. source toward the southwest. A comparison of high and low resolution images shows that this emission appears to be composed of several synchrotron clumps which are surrounded by diffuse emission. The eastern extension beyond the Parma et al. source is composed of three clumps of emission which are connected to the main source by a faint synchrotron bridge. Spectral index images of the emission reveal a steepening of the spectrum away from the radio core.

A morphological comparison of the radio and X-ray emission in Abell 262 shows a significant interaction in the cluster core. The innermost of the newly identified eastern radio structures falls at the position of a low significance X-ray deficit identified by Blanton et al. (2004). The other two outer eastern radio features appear to be associated with a newly discovered X-ray depression. The western radio emission completely fills the newly discovered X-ray tunnel seen in our residual *Chandra* image. Similar X-ray tunnels filled with low frequency emission are seen in Abell 2597 (Clarke et al. 2005) and

Perseus (Fabian et al. 2006). These tunnels may represent regions where multiple radio outbursts pile up and accumulate over several AGN activity cycles.

The integrated radio spectrum of B2 0149+35 shows evidence of spectral steepening to high frequencies. Using three particle injection models (Jaffe-Perola, Karsashev-Pacholczyk, and continuous injection), we estimate the break frequency to be between 1400 and 9600 MHz. Under the source field strength assumption given in Section 4.3, this range of break frequencies leads to upper limits on the radiative age of the source of between 47 and 18 Myr. Minimum energy synchrotron arguments yield a synchrotron lifetime of  $\sim 37$  Myr for the source at frequencies around 1400 MHz. These timescales can be compared to the buoyancy timescale ( $\tau_{buoy} \gtrsim 80$  Myr) calculated assuming that the western lobe is from a past outburst and that it detached and rose buoyantly to the end of the X-ray tunnel. From this comparison, it is not clear whether active particle injection or particle acceleration is required within the tunnel to maintain the observed radio emission due to the large uncertainties in the synchrotron age (§4.1) and buoyancy timescale (§4.2). We have also used the projected separation of the eastern clumps of emission in the buoyancy model (assuming the lobes rise at the terminal velocity) to estimate a lower limit of  $\tau_{rep}=28$  Myr on the average repetition rate of outbursts for the central AGN.

The X-ray pressure surrounding the extended radio emission is estimated to be more than 25 times larger than the minimum energy synchrotron pressure calculated if we assume a synchrotron filling factor of unity and equal energy in relativistic ions and electrons. This discrepancy may suggest that the radio lobes are fed by heavy, baryon-dominated plasma. Alternatively there may be an additional form of pressure support within the radio lobes.

The total energy input into the ICM of Abell 262 over multiple outburst episodes was calculated by assuming that each radio component to the east of the core represents a lobe from an AGN outburst. In this model the western emission filling the tunnel would be the result of a series of overlapping buoyant lobes. The total energy input over the 4 outbursts is estimated to be  $2.2 \times 10^{58}$  ergs. By comparison, the outburst in clusters such as Abell 2052 (Blanton et al. 2009) and Perseus

(Fabian et al. 2000) ranges from a few times  $10^{58}$  to a few times  $10^{59}$  ergs. The most powerful known radio outburst is in MS0735.6+7421 with an estimated energy of  $6 \times 10^{61}$  ergs (McNamara et al. 2005).

We compared the lower limit on the AGN energy input into the ICM to the bolometric radio luminosity of B2 0149+35 to estimate a radiative efficiency of  $\epsilon = 0.001$ . This efficiency agrees well with that previously calculated for this system by Birzan et al. (2004).

Although previous measurements of the kinetic radio power of B2 0149+35 indicated that the current outburst was too weak to offset the radiative cooling, our new measurements suggest that the source can approximately offset the radiative cooling on average over the four observed outburst episodes.

The ubiquitous nature of low frequency radio emission as a chronicle of recent and past AGN activity in clusters underscores the importance of emerging instruments such as LOFAR and the LWA for delineating the role of AGN feedback in the ICM.

The National Radio Astronomy Observatory (NRAO) is a facility of the National Science Foundation operated under cooperative agreement by Associated Universities, Inc. We thank the staff of the GMRT that made these observations possible, and Samir Dhurde in particular for his assistance. GMRT is run by the National Centre for Radio Astrophysics of the Tata Institute of Fundamental Research. The Digitized Sky Surveys were produced at the Space Telescope Science Institute under U.S. Government grant NAG W-2166. The images of these surveys are based on photographic data obtained using the Oschin Schmidt Telescope on Palomar Mountain and the UK Schmidt Telescope. Basic research in radio astronomy at the NRL is supported by 6.1 Base funding. TEC was supported in part by the National Aeronautics and Space Administration through *Chandra* awards GO6-7115B, and GO7-8132B. ELB was supported in part by the National Aeronautics and Space Administration through *Chandra* award G07-8132A and a Clare Boothe Luce Professorship. CLS was supported in part by the National Aeronautics and Space Administration through *Chandra* awards GO5-6081X, GO5-6126X, and AR7-8012X.

## REFERENCES

- Andernach, H., Waldthausen, H., & Wielebinski, R. 1980, *A&AS*, 41, 339
- Ballarati, B., Nanni, M., Feretti, L., Giovannini, G., & Gavazzi, G. 1983, *A&AS*, 51, 321
- Bernardi, M., Alonso, M. V., da Costa, L. N., Willmer, C. N. A., Wegner, G., Pellegrini, P. S., Rit e, C., & Maia, M. A. G. 2002, *AJ*, 123, 2990
- Bicknell, G. V. 1995, *ApJS*, 101, 29
- Birzan, L., McNamara, B. R., Nulsen, P. E. J., Carilli, C. L., & Wise, M. W. 2008, *ApJ*, 686, 859
- Birzan, L., Rafferty, D. A., McNamara, B. R., Wise, M. W., & Nulsen, P. E. J. 2004, *ApJ*, 607, 800
- Blanton, E. L., Clarke, T. E., Anderson, L. D., Douglass, E. M., & Sarazin, C. L. 2009, in preparation
- Blanton, E. L., Sarazin, C. L., McNamara, B. R., & Clarke, T. E. 2004, *ApJ*, 612, 817
- Boehringer, H., Voges, W., Fabian, A. C., Edge, A. C., & Neumann, D. M. 1993, *MNRAS*, 264, L25
- Burns, J. O. 1990, *AJ*, 99, 14
- Cardiel, N., Gorgas, J., & Aragon-Salamanca, A. 1998, *MNRAS*, 298, 977
- Churazov, E., Brüggen, M., Kaiser, C. R., Böhringer, H., & Forman, W. 2001, *ApJ*, 554, 261
- Churazov, E., Sunyaev, R., Forman, W., Böhringer, H. 2002, *MNRAS*, 332, 729
- Clarke, T., Blanton, E., Sarazin, C., Kassim, N., Anderson, L., Schmitt, H., Gopal-Krishna, & Neumann, D. 2007, in *Heating Versus Cooling in Galaxies and Clusters of Galaxies*, ed. H. Böhringer, G. W. Pratt, A. Finoguenov, & P. Schuecker (Berlin: Springer-Verlag), 124
- Clarke, T. E., Sarazin, C. L., Blanton, E. L., Neumann, D. M., & Kassim, N. E. 2005, *ApJ*, 625, 748
- Cohen, A. S., Lane, W. M., Cotton, W. D., Kassim, N. E., Lazio, T. J. W., Perley, R. A., Condon, J. J., & Erickson, W. C. 2007, *AJ*, 134, 1245
- Colla, G., et al. 1973, *A&AS*, 11, 291
- Conroy, C., & Ostriker, J. P. 2008, *ApJ*, 681, 151
- Cowie, L. L., & Binney, J. 1977, *ApJ*, 215, 723



- Crawford, C. S., Allen, S. W., Ebeling, H., Edge, A. C., & Fabian, A. C. 1999, *MNRAS*, 306, 857
- De Young, D. S. 1993, *ApJ*, 405, L13
- Diehl, S., Li, H., Fryer, C. L., & Rafferty, D. 2008, *ApJ*, 687, 173
- Douglas, J. N., Bash, F. N., Bozayan, F. A., Torrence, G. W., & Wolfe, C. 1996, *AJ*, 111, 1945
- Dunn, R. J. H., & Fabian, A. C. 2004, *MNRAS*, 355, 862
- Dunn, R. J. H., Fabian, A. C., & Sanders, J. S. 2006, *MNRAS*, 366, 758
- Dunn, R. J. H., Fabian, A. C., & Taylor, G. B. 2005, *MNRAS*, 364, 1343
- Fabian, A. C., Celotti, A., Blundell, K. M., Kassim, N. E., & Perley, R. A. 2002, *MNRAS*, 331, 369
- Fabian, A. C., & Nulsen, P. E. J. 1977, *MNRAS*, 180, 479
- Fabian, A. C., Sanders, J. S., Allen, S. W., Crawford, C. S., Iwasawa, K., Johnstone, R. M., Schmidt, R. W., & Taylor, G. B. 2003, *MNRAS*, 344, L43
- Fabian, A. C., et al. 2000, *MNRAS*, 318, L65
- Fabian, A. C., Sanders, J. S., Taylor, G. B., Allen, S. W., Crawford, C. S., Johnstone, R. M., & Iwasawa, K. 2006, *MNRAS*, 366, 417
- Forman, W., et al. 2007, *ApJ*, 665, 1057
- Gitti, M., Feretti, L., & Schindler, S. 2006, *A&A*, 448, 853
- Gregory, P. C., Scott, W. K., Douglas, K., & Condon, J. J. 1996, *ApJS*, 103, 427
- Gopal-Krishna, & Saripalli, L. 1984, *A&A*, 141, 61
- Hales, S. E. G., Baldwin, J. E., & Warner, P. J. 1993, *MNRAS*, 263, 25
- Hardcastle, M. J., & Worrall, D. M. 2000, *MNRAS*, 319, 562
- Heinz, S., Brügggen, M., Young, A., & Levesque, E. 2006, *MNRAS*, 373, L65
- Jaffe, W. J., & Perola, G. C. 1973, *A&A*, 26, 423
- Kardashev, N. S. 1962, *Soviet Astronomy*, 6, 317
- Kaastra, J. S., Ferrigno, C., Tamura, T., Paerels, F. B. S., Peterson, J. R., & Mittaz, J. P. D. 2001, *A&A*, 365, L99
- Lal, D. V., & Rao, A. P. 2006, *MNRAS*, in press
- Lane, W. M., Clarke, T. E., Taylor, G. B., Perley, R. A., & Kassim, N. E. 2004, *AJ*, 127, 48
- Laing, R. A., Riley, J. M., & Longair, M. S. 1983, *MNRAS*, 204, 151
- McNamara, B. R., & Nulsen, P. E. J. 2007, *ARA&A*, 45, 117
- McNamara, B. R., Nulsen, P. E. J., Wise, M. W., Rafferty, D. A., Carilli, C., Sarazin, C. L., & Blanton, E. L. 2005, *Nature*, 433, 45
- McNamara, B. R., & O'Connell, R. W. 1989, *AJ*, 98, 2018
- Miley, G. 1980, *ARA&A*, 18, 165
- Nulsen, P. E. J., McNamara, B. R., Wise, M. W., & David, L. P. 2005, *ApJ*, 628, 629
- Owen, F. N., Eilek, J. A., & Kassim, N. E. 2000, *ApJ*, 543, 611
- Pacholczyk, A. G. 1970, *Series of Books in Astronomy and Astrophysics*, San Francisco: Freeman, 1970
- Parma, P., de Ruiter, H. R., Fanti, C., & Fanti, R. 1986, *A&AS*, 64, 135
- Peterson, J. R., et al. 2001, *A&A*, 365, L104
- Peterson, J. R., Kahn, S. M., Paerels, F. B. S., Kaastra, J. S., Tamura, T., Bleeker, J. A. M., Ferrigno, C., & Jernigan, J. G. 2003, *ApJ*, 590, 207
- Plana, H., Boulesteix, J., Amram, Ph., Carignan, C., & Mendes de Oliveira, C. 1998, *A&AS*, 128, 75
- Rafferty, D. A., McNamara, B. R., Nulsen, P. E. J., & Wise, M. W. 2006, *ApJ*, 652, 216
- Rudnick, L. & Owen, F. N. 1977, *AJ*, 82, 1
- Sakelliou, I., et al. 2002, *A&A*, 391, 903
- Tamura, T., et al. 2001, *A&A*, 365, L87
- Tremaine, S., et al. 2002, *ApJ*, 574, 740
- van der Laan, H., & Perola, G. C. 1969, *A&A*, 3, 468
- Vikhlinin, A., Kravtsov, A., Forman, W., Jones, C., Markevitch, M., Murray, S. S., & Van Speybroeck, L. 2006, *ApJ*, 640, 691
- White, R. L., & Becker, R. H. 1992, *ApJS*, 79, 331
- Wise, M. W., McNamara, B. R., Nulsen, P. E. J., Houck, J. C., & David, L. P. 2007, *ApJ*, 659, 1153
- Wold, M., Lacy, M., & Armus, L. 2007, *A&A*, 470, 531
- Wong, K.-W., Sarazin, C. L., Blanton, E. L., & Reiprich, T. H. 2008, *ApJ*, 682, 155

TABLE 1  
 RADIO OBSERVATIONS OF B2 0149+35

Date	Instrument/Array	Frequency (MHz)	Bandwidth (MHz)	Duration (hours)	Obs. Code
1997 Sep 18	VLA/C	1364.9/1435.1	50/50	0.6	AC488
2000 Oct 01	VLA/D	4535.1	50	0.4	AC557
2000 Dec 19	VLA/A	1365/1415.5	25/25	0.4	AC572
2000 Dec 19	VLA/A	1465/1515	25/25	0.4	AC572
2003 Jul 27	VLA/A	321.5/328.5	6.3/6.3	3.5	AC682
2004 Jul 24	GMRT	240	8.0	8.5	06TEC01
2004 Jul 24	GMRT	606/622	16/16	8.5	06TEC01
2005 Apr 16	VLA/B	1396.5	6.3	1.7	AM828

TABLE 2  
FLUX MEASUREMENTS

Frequency (MHz)	Flux (mJy)	Reference
74	1060±140	1
151	780± 207	2
235	392± 20	3
365	339± 38	4
328	288± 4	3
408	364± 66	5
408	240± 70	6
613	198± 10	3
1365	92± 2	3
1400	131± 30	7
2695	48± 6	8
4535	27± 1	3
4850	40± 10	9
4850	32± 4	10

REFERENCES. — (1) Cohen et al. 2006; (2) Hales et al. 1993; (3) This work; (4) Douglas et al. 1996; (5) Colla et al. 1973; (6) Ballarati et al. (1983); (7) White & Becker 1992; (8) Rudnick & Owen 1977; (9) Andernach et al. 1980; (10) Gregory et al. 1996.

TABLE 3  
BUBBLE ENERGIES

Bubble	a	b	r	$E_o$
(1)	(kpc) (2)	(kpc) (3)	(kpc) (4)	( $10^{56}$ ergs) (5)
A	5.56	4.99	8	82
B	5.56	4.99	10	68
C	4.16	4.16	18	25
D	5.10	3.37	20	20
E	3.48	2.39	25	6.1
F	3.76	2.04	26	4.7
G	4.58	3.19	29	13

NOTE. — Col.(1): Bubble ID as indicated in Figure 7. Col.(2): Projected semimajor axis of bubble. Col.(3) Projected semiminor axis of bubble. Col.(4) Bubble-center projected radial distance from the core of B2 0149+35. Col.(5) Initial AGN outburst energy required to create bubble.

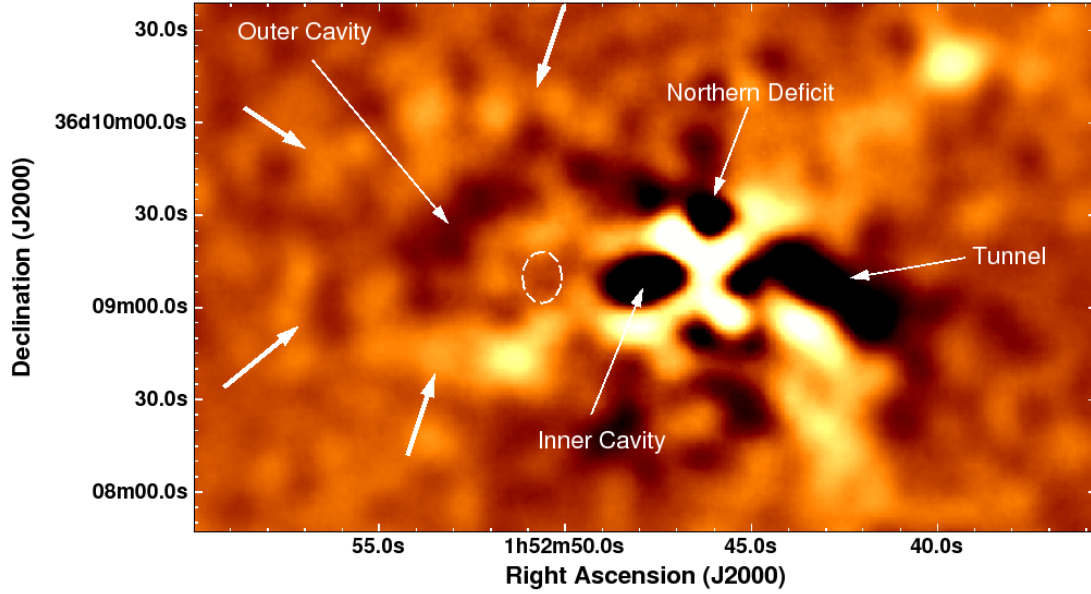


FIG. 1.— Residual *Chandra* image of the central region ( $96 \times 56$  kpc) of Abell 262, produced by subtracting an elliptical isophotal model from the merged  $\sigma=5''$  Gaussian smoothed image in the  $0.3 - 10$  keV band. The eastern X-ray cavity and newly discovered western tunnel are the most prominent features of the image. To the north of the cluster core there is an X-ray deficit located between two bright regions which are coincident with [N II] emission. The dashed ellipse indicates the position of the faint X-ray depression discussed in Blanton et al. (2004). The new deep residual image also hints to the presence of an extended deficit to the east of the dashed ellipse which may be surrounded by a faint rim. The labels indicate the deficits while the thick arrows mark the rough location of the faint eastern rim.

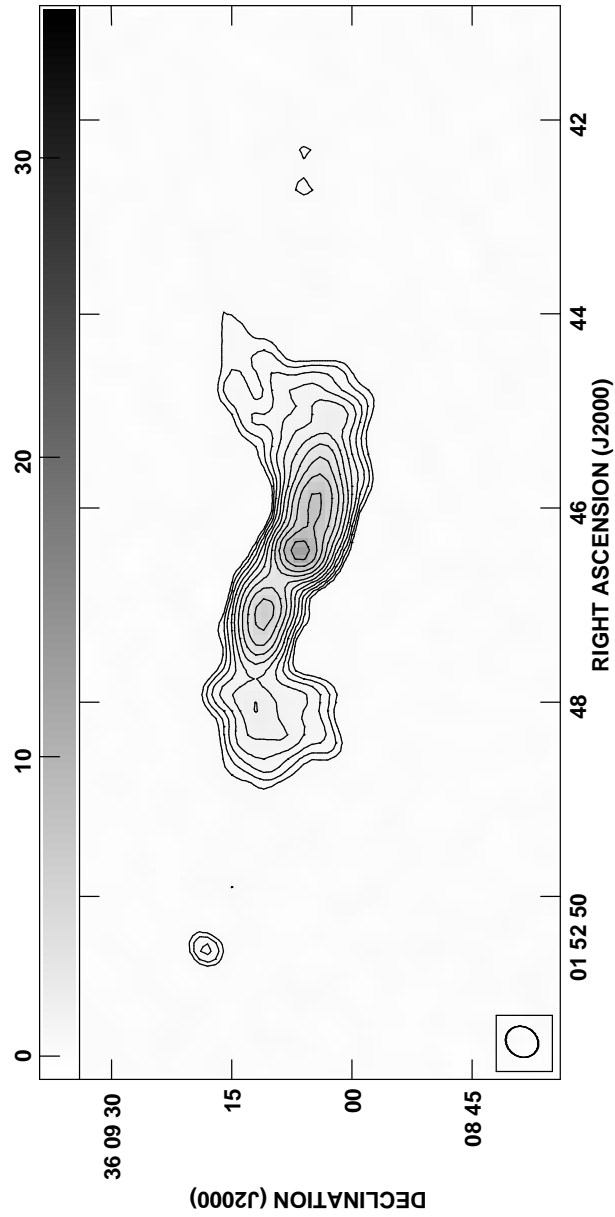


FIG. 2.— NRAO VLA image at 1400 MHz of B2 0149+32. The resolution of the image is  $4''.2 \times 3''.7$  (the beam is shown in the lower left corner of the image), and the contours increase by  $\sqrt{2}$  from  $3\sigma$  where  $\sigma=0.11$  mJy/beam. The bar at the top of the image shows the total intensity scale in units of mJy/beam. The compact source at RA(J2000)=01 52 50.5, Dec(J2000)=36 09 18.18 may be an unrelated background source.

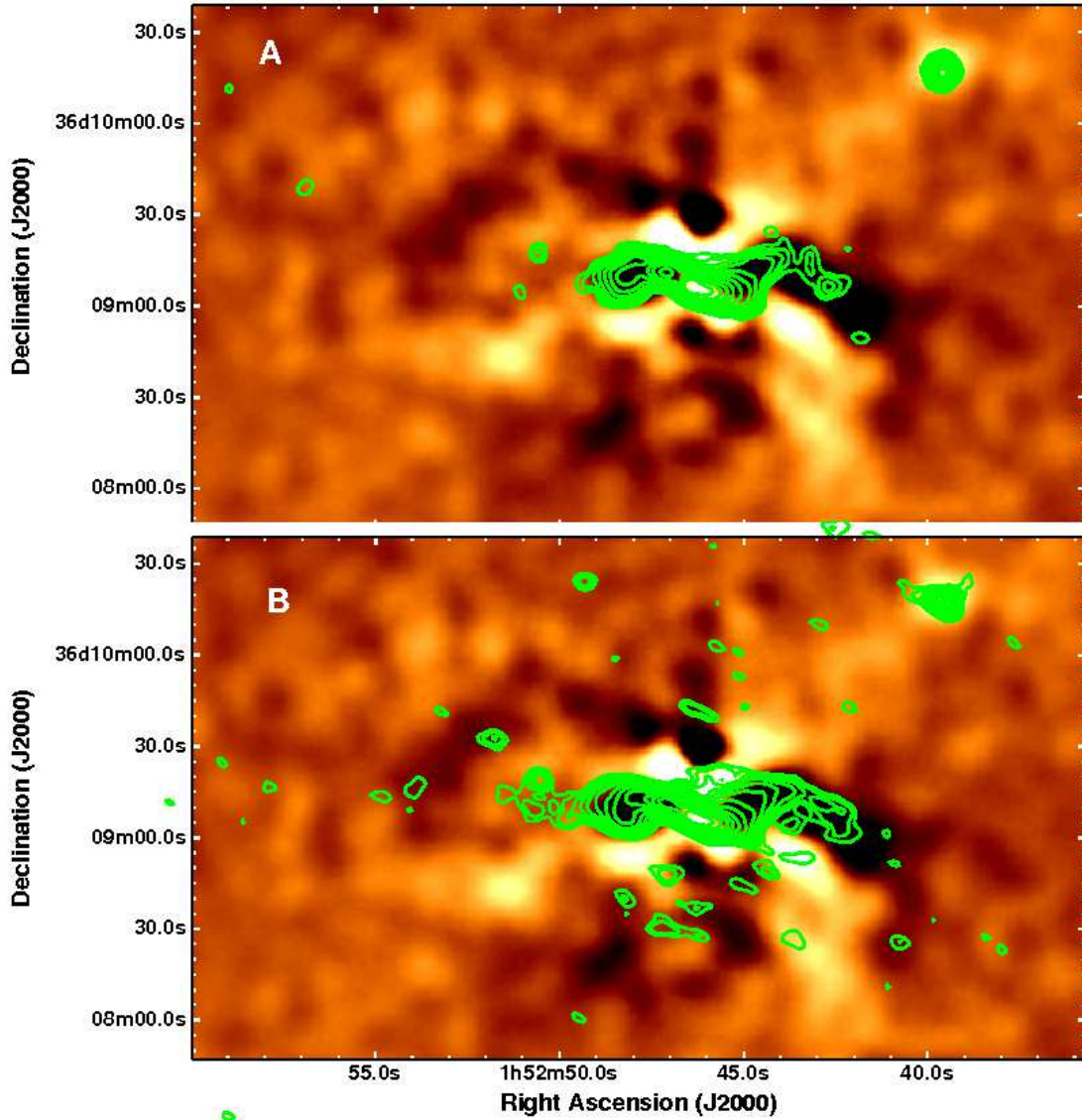


FIG. 3.— **A**: Combined A, B and C configuration VLA image at 1400 MHz of B2 0149+32 overlaid as contours on the residual *Chandra* image (Figure 1). The resolution of the radio image is  $6''.0 \times 5''.5$  and the contours increase by  $\sqrt{2}$  from  $3\sigma$ , where  $\sigma=0.12$  mJy/bm. The radio emission associated with NGC708 is seen to extend further to the west along a tail that runs to the southwest along the X-ray tunnel. **B**: Full resolution GMRT 610 MHz radio contours overlaid on the residual *Chandra* image. The radio data have a resolution of  $5''.9 \times 4''.6$  and the contours increase by  $\sqrt{2}$  from  $3\sigma$ , where  $\sigma=0.11$  mJy/bm. The radio emission traces further along the X-ray tunnel than seen at 1400 MHz and also shows evidence of a radio extension to the east which is coincident with the faint X-ray depression discussed in Blanton et al. (2004).

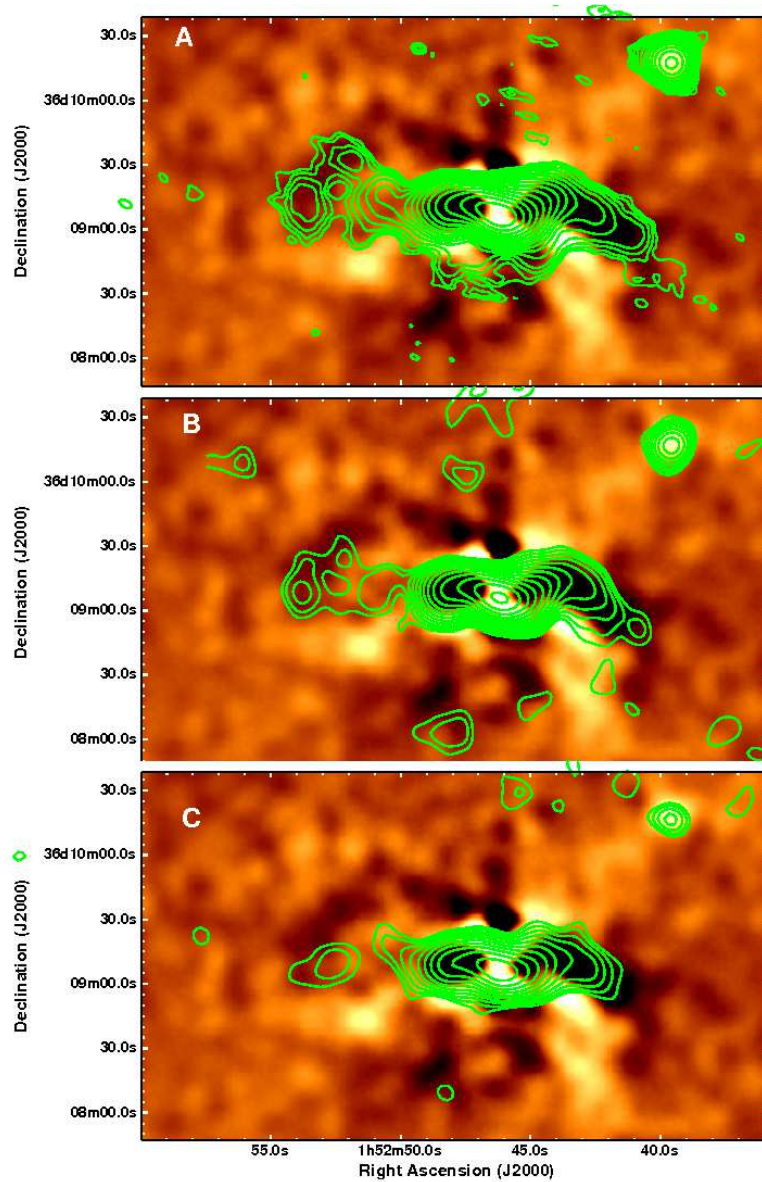


FIG. 4.— Residual X-ray image of Abell 262 (Figure 1) with radio contours overlaid. **A:** Tapered GMRT 610 MHz data where the data have been weighted to produce an image at lower resolution ( $\theta=13''.1 \times 13''.1$ ) that is more sensitive to lower surface brightness emission. The radio contours increase by  $\sqrt{2}$  from  $3\sigma$ , where  $\sigma=0.12$  mJy/bm. The radio emission traces the full length of the southwest tunnel and shows evidence of a series of connected clumps to the east which are coincident with the newly detected extended eastern deficit. **B:** The radio contours show the VLA 330 MHz radio emission plotted for the two sigma contour and higher ( $\sigma=0.66$  mJy/bm,  $\theta=13''.1 \times 13''.1$ ). Although this data is not as sensitive as the 610 MHz GMRT data it shows the same morphology of the radio emission along the tunnel as well as the clumps associated with the extended eastern deficit. **C:** The GMRT 235 MHz radio emission is less sensitive than the other frequencies but still shows the radio emission tracing the length of the southwest tunnel and some clumpy emission in the southern part of the eastern deficit. The resolution at 235 MHz is  $\theta=13''.1 \times 13''.1$  and the contours increase by  $\sqrt{2}$  from  $3\sigma$ , where  $\sigma=1.1$  mJy/bm.



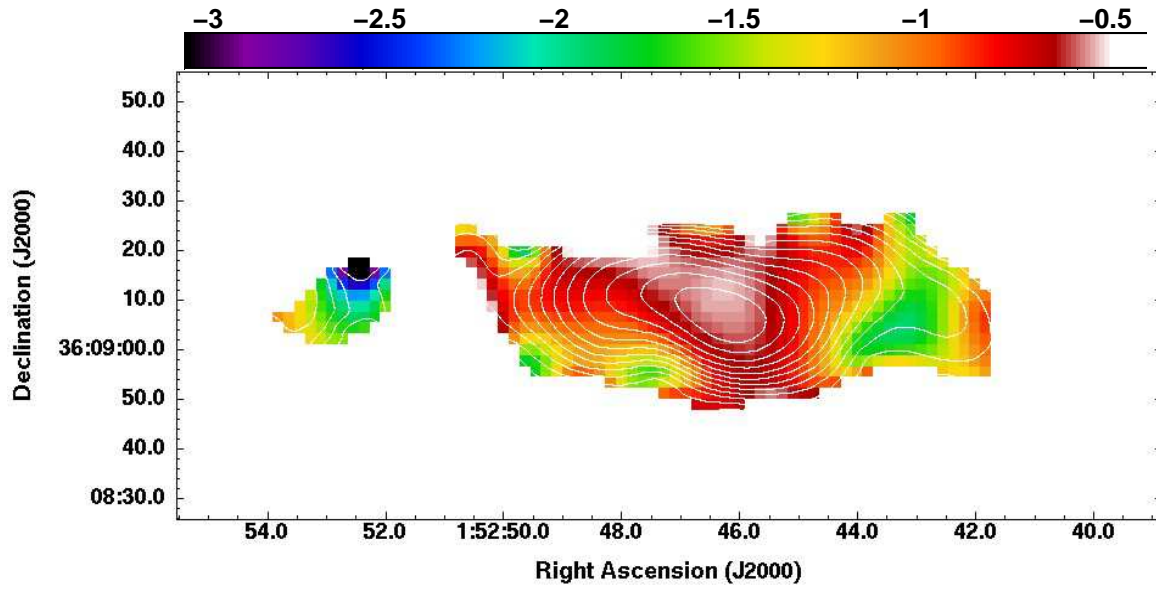


FIG. 5.— Spectral index map between 235 and 610 MHz. The 610 MHz total intensity contours are overplotted to help connect the spectral properties to the morphology. The core shows a relatively flat spectral index ( $\alpha = -0.5$ ). The spectrum shows significant steepening away from the core to the west as well as a smaller spectral steepening away from the core to the east.

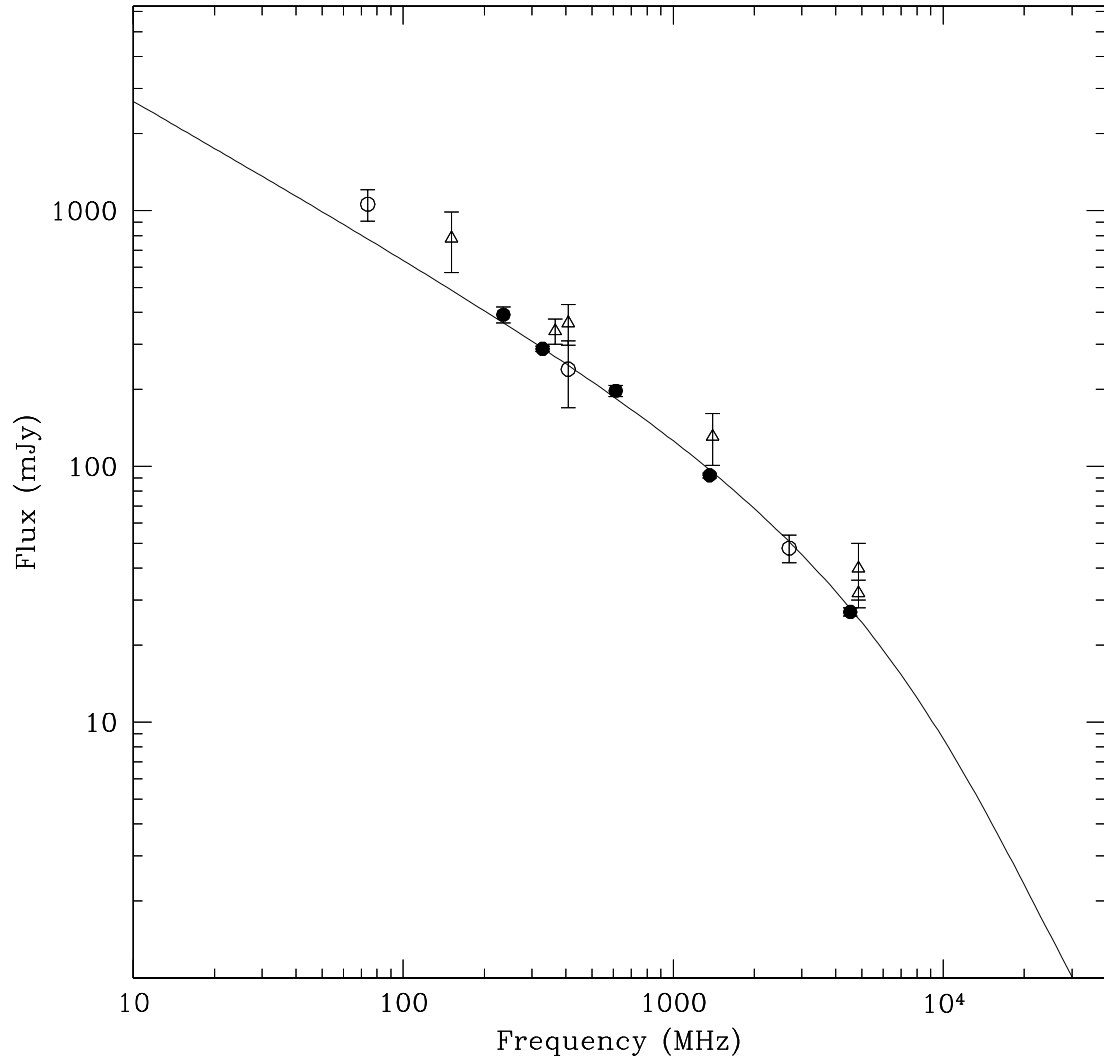


FIG. 6.— Integrated radio flux measurements for Abell 262 from this paper as well as the literature. Filled circles show the data points from this work and open symbols represent measurements taken from the literature. The open circles are from observations with sufficient resolution to separate the emission of the central radio source from the neighboring sources while the open triangles are low resolution observations which likely contain contamination from the nearby sources. The solid line shows the best-fit KP spectral model.

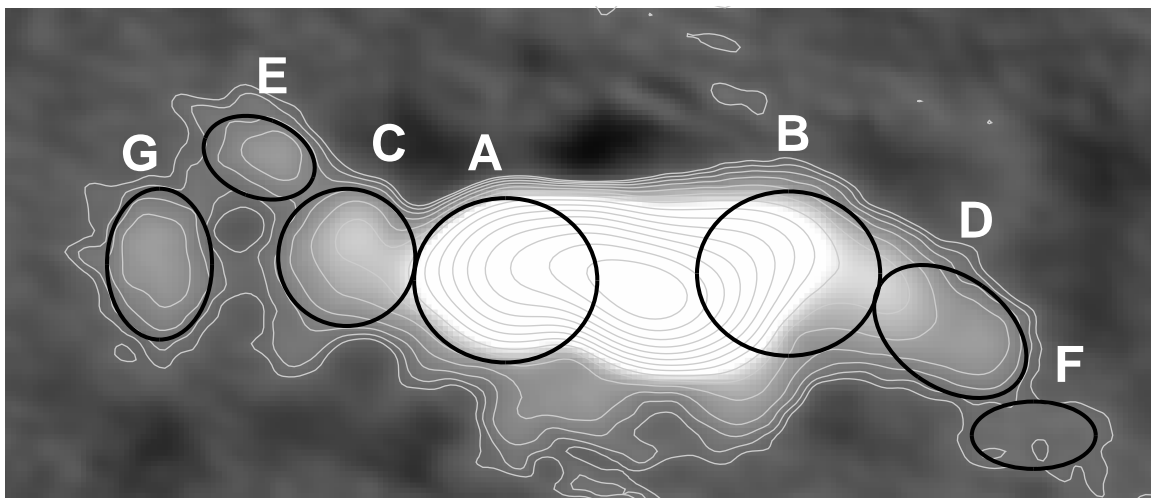


FIG. 7.— Tapered GMRT 610 MHz image with individual source components shown as overlaid black ellipses. Each component was identified based on the radio morphology of the source.